



Reaction and transport in Ag/Ag₂O gas diffusion electrodes of aqueous Li–O₂ batteries: Experiments and modeling



Timo Danner ^{a,b,c,d,*}, Birger Horstmann ^{a,b,c}, Dennis Wittmaier ^a, Norbert Wagner ^a, Wolfgang G. Bessler ^{b,d}

^a German Aerospace Center (DLR), Institute of Technical Thermodynamics, Stuttgart, Germany

^b University of Stuttgart, Institute for Thermodynamics and Thermal Engineering, Stuttgart, Germany

^c Helmholtz Institute Ulm for Electrochemical Energy Storage (HIU), Ulm, Germany

^d Institute of Energy System Technology (INES), Offenburg University of Applied Sciences, Offenburg, Germany

HIGHLIGHTS

- We model aqueous lithium–oxygen batteries.
- Multiphase-flow in porous gas diffusion electrodes is important.
- We perform half-cell experiments for validation and parameterization.
- We identify rate-limiting processes via sensitivity analysis.

ARTICLE INFO

Article history:

Received 4 February 2014

Received in revised form

11 February 2014

Accepted 24 March 2014

Available online 26 April 2014

Keywords:

Lithium–oxygen (Li–O₂)

Aqueous electrolyte (LiOH)

Half-cell experiments

Modeling and simulation

Electrode design

ABSTRACT

Aqueous lithium–oxygen batteries are promising candidates for electric energy storage. In this paper we present and discuss a multiphase continuum model of an aqueous lithium–oxygen single cell including reactions and transport in a porous gas diffusion electrode (GDE). The model is parameterized using in-house half-cell experiments and available literature data on aqueous electrolytes. We validate our transport model with cyclic voltammetry and electrochemical impedance spectroscopy measurements over a wide range of temperatures (25, 40, 55 °C) and electrolyte concentrations (0.1–2 M). We observe very good agreement between simulations and measurements during oxygen reduction conditions. A sensitivity analysis of the validated model demonstrates the influence of the porous structure on GDE performance and gives directions for the future development of electrodes.

© 2014 Elsevier B.V. All rights reserved.

1. Introduction

Recent years showed a strong public interest in the topic of battery-powered electric vehicles. However, the energy density of state-of-the-art lithium-ion technology [1–3] is not sufficient to reach driving ranges comparable to those of cars with conventional combustion engines. Therefore, a focus of research turned to so called post-lithium-ion technologies, including lithium–sulfur (Li–S) and lithium–oxygen (Li–O₂) [3]. Li–O₂ batteries [4–7] are particularly interesting due to their very high theoretical energy density. Still, there are many challenges in the development of this

type of battery [8], including insufficient cycling efficiency and lifetime.

Research on metal–air batteries (Zn–O₂, Li–O₂, Al–O₂, Mg–O₂, etc.) using aqueous electrolytes started in the early 1960s [9]. The many practical problems associated with the technology, however, obviated a successful development other than for small primary cells. A renewed interest grew when Abraham et al. [10] demonstrated the use of organic electrolytes in Li–O₂ batteries. During discharge the solid reaction product Li₂O₂ is supposed to form in the porous structure of the cathode:



In this case, the capacity of the Li–O₂ cell is limited by the low conductivity of Li₂O₂ [11–15] and an insufficient supply of oxygen through the pore space [16–19]. However, the standard electrolyte

* Corresponding author. Helmholtz Institute Ulm, Albert-Einstein-Allee 11, 89069 Ulm, Germany. Tel.: +49 (0)731 50 34306; fax: +49 (0)731 50 34011.

E-mail address: Timo.Danner@DLR.de (T. Danner).

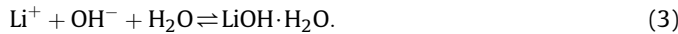
used in lithium-ion technology were found to be unstable in $\text{Li}-\text{O}_2$ batteries [7,20,21]. Thus, the focus of research currently concentrates on finding a suitable and stable organic electrolyte [22–24].

Aqueous electrolyte systems offer an interesting alternative [25]. The lithium salt solutions used in aqueous electrolytes are highly conductive [26] and, most importantly, the alkaline environment offers reversible electrochemistry over a wide potential window. The oxygen reduction reaction (ORR) [27] and oxygen evolution reaction (OER) in alkaline media are given by



At the anode lithium metal is typically used to attain high energy densities. However, lithium reacts vigorously with water. A challenge for this system is therefore the development of a water-impermeable separator which is stable towards lithium and the alkaline electrolyte [28]. Several groups dedicated their efforts to this topic and demonstrated stable operation over a large number of cycles [29–31].

During discharge, the concentrations of Li^+ and OH^- ions increase until the solubility limit is reached and solid $\text{LiOH}\cdot\text{H}_2\text{O}$ precipitates in the battery according to



This can cause problems similar to the aprotic system, that is, pore clogging and coverage of active surfaces. Yet, solid discharge products are necessary to reach high energy densities. The two-step mechanism of aqueous-electrolyte cells (Eqs. (2) and (3)) offers interesting design options, as charge transfer and precipitation can be spatially separated in contrast to organic-electrolyte cells (Eq. (1)). For example, the problem of pore clogging can be solved by the use of bulk separators as proposed by Stevens et al. and Horstmann et al. [32,33]. Here, the anode protective layer (APL) can be coated with a polymer such that the precipitates accumulate on the bottom of the separator. This way the solid products do not block or passivate the GDE and higher capacities can be reached.

The cathode material and design is of key importance for cell functionality. In the present work, we propose and demonstrate the use of gas diffusion electrodes (GDE) for aqueous $\text{Li}-\text{O}_2$ cells. GDEs allow attaining high power densities which are necessary for the propulsion of electric vehicles. A GDE usually consists of a porous catalyst layer (CL) which is placed on a support material such as a metal mesh for mechanical stability. The coexistence of gas and liquid phases in the porous structure ensures a fast transport of oxygen and a large specific surface area.

The saturation management is of utmost importance for the successful operation of the GDE as it determines the transport within the porous network. On the one hand a dry operation will hamper GDE performance due to insufficient transport of the reactants in the liquid phase. On the other hand a flooded electrode limits the transport of oxygen to the active sites. The development of $\text{Li}-\text{O}_2$ cathodes benefits from the extensive work done on this topic in fuel cell research [34]. Here, many studies deal with the transport and water management in gas diffusion layers (GDLs) of polymer electrolyte membrane fuel cells (PEMFCs) [35–41].

Mathematical models are very helpful for understanding the interplay of transport and kinetics in these complex systems. Thus, a validated continuum model has to be regarded as an important tool which allows a concerted development of GDE structure and properties in order to optimize its performance. First models on transport in GDEs of alkaline fuel cells were developed on the assumption of thin electrolyte films [42] within the porous electrode. This was later extended to the model of flooded

agglomerates [43]. A good agreement with experimental findings was reported [44] for the latter type.

In this work we follow a twofold approach to increase understanding of relevant processes in GDEs of aqueous $\text{Li}-\text{O}_2$ batteries. We perform half-cell experiments in a three-electrode setup with commercial Ag_2O electrodes [45]. The extensive parameter field is then used to parameterize and validate a 1D continuum model. The model includes electrochemical reactions, multi-phase transport in the GDE, as well as solid precipitation. This paper is structured as follows: In the first part of this article we explain the measurement setup and give an overview of experimental findings (Section 2). In Section 3 we present a 1D continuum model of a GDE operating in aqueous LiOH solutions. The model is parameterized (Section 4.1) and validated (Section 4.2) based on data from the literature and our own experiments. The validated model is then used in Section 4.3 for the identification and discussion of important parameters, such as porosity, tortuosity or electrode thickness, in order to improve the performance of the GDE.

2. Experiments

2.1. Experimental setup

We used a silver/silver oxide electrode from Bayer Material Science [45] for our measurements. The electrode was made up of a nickel mesh and a catalyst layer consisting of Ag_2O , Ag, and PTFE. The total thickness of the electrode was $\sim 560 \mu\text{m}$. An electron micrograph of the cross-section through the electrode is shown in Fig. 1. The inset on the right shows a close-up view of the porous structure in the catalyst layer. The thin connecting fibers stem from the hydrophobic binder and ensure the coexistence of a gas and a liquid phase in the void volume. The electrode was structurally characterized using mercury intrusion porosimetry and krypton adsorption measurements (Porotec). Structural parameters are listed in Table 1. The experimental setup is described in detail in Ref. [46].

Aqueous solutions of LiOH were prepared from $\text{LiOH}\cdot\text{H}_2\text{O}$ (98% Alpha Aesar) and demineralized water at room temperature (0.1, 0.2, 1 and 2 M). The cell was operated under purified oxygen atmosphere at atmospheric pressure. A SGL 35DC gas diffusion layer (Sigracet) was used to prevent leakage of the electrolyte into the gas channel. The temperature of the electrolyte solution was controlled via a water bath. We used the HydroFlex electrode (RHE, Gaskatel) as reference electrode directly in the electrolyte solution. An IM-6 Electrochemical Workstation (Zahner) controlled the electrochemical measurements.

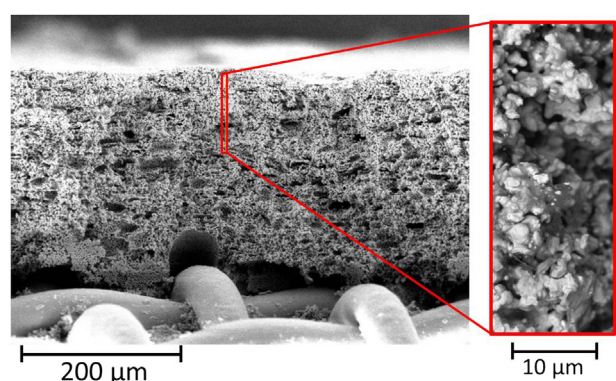


Fig. 1. Electron microscope image of an Ag_2O gas diffusion electrode studied in this work. The inset shows a close-up image of the microstructure of the catalyst layer. Smaller particles are connected by thin filaments forming larger agglomerates. The thin filaments originate from the hydrophobic binder.

Table 1

Summary of geometrical and structural parameters for each modeling domain. Initial values for saturation in the cathode (volume fraction of gas and electrolyte) and electrolyte composition change due to different operating conditions.

Cathode	Thickness (L_{GDE})	560 μm
	Discretization points	30
	Porosity	0.48
	Mean pore diameter	1 μm
	Phases	Species
	Conductor	e^-
	Gas	$O_2^{(\text{gas})}$
Electrolyte	Electrolyte	$H_2O, OH^-, Li^+, O_2^{(\text{aq})}$
	Thickness (L_{EB})	10 cm
	Discretization points	10
	Sample holder (L_{SH})	2 cm ($\gamma = 30^\circ$)
	Reference electrode (L_{ref})	5 mm
	Porosity	1
	Phases	Species
Anode	Electrolyte	$H_2O, OH^-, Li^+, O_2^{(\text{aq})}$
	Thickness	100 μm
	Discretization points	1
	Porosity	0.99
	Phases	Species
	Conductor	e^-
	Electrolyte	$H_2O, OH^-, Li^+, O_2^{(\text{aq})}$
Atmosphere	Phases	Species
	Gas	$O_2^{(\text{gas})}$

2.2. Electrochemical characterization

Measurements for oxygen reduction and oxygen evolution at a fixed electrolyte concentration were consecutively performed with the same electrode and in the same electrolyte solution. Prior to the measurements we fully reduced the electrode at 500 mV vs. RHE [46]. This ensured a characterization under stable conditions. First we recorded cyclic voltammograms and electrochemical impedance spectra for the ORR at 25, 40, and 55 °C. After these measurements we fully oxidized the electrode at a voltage of 1850 mV vs. RHE and reran the same protocol under oxygen evolution conditions. Finally, we repeated the CV measurements at 55 °C in the ORR regime in order to check the electrode for possible degradation. A fresh electrode of the same batch was used for each concentration. In the following Sections 2.2.1 and 2.2.2 we discuss the typical features of cyclic voltammograms and impedance spectra of the porous Ag GDE. Measurements at different concentrations showed qualitatively similar results. Therefore, we restrict our discussion on the measurements in 1 M LiOH solution. Results at other concentrations are shown in the course of model validation in Section 4.2.

2.2.1. Cyclic voltammetry

As mentioned above, cyclic voltammograms were recorded separately in the ORR and OER regime. The potential range covered was 1100 mV–500 mV (ORR) and 1400 mV–1950 mV (OER), respectively. In order to avoid significant double layer currents, we chose a slow scan rate of 1 mV s⁻¹.

The cyclic voltammograms for the ORR are shown in Fig. 2 at potentials below 1.1 V vs. RHE. After an initial drop, the cathodic current stabilized at a small value. At even lower potential the current linearly increased with overpotential during the forward scan. A rise in temperature led to steeper slopes in the linear region. The maximum current was drawn at the turning point of the potential scan. Below potentials of 1 V the forward and the backward sweep collapsed onto a single line. The initial drop in

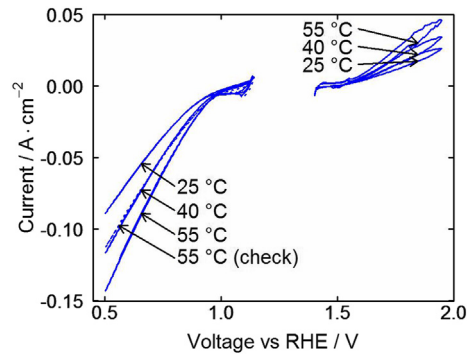


Fig. 2. Experimental cyclic voltammograms under oxygen reduction (0.5–1.1 V) and oxygen evolution (1.4–1.95 V) conditions at 25, 40 and 55 °C. The collapsing lines of forward and backward scan under oxygen reduction demonstrate a negligible influence of the double layer current and a good transport of reactants. The dotted line refers to a repeated measurement of a cathodic cycle at 55 °C after operating the electrode under oxygen evolution conditions. The lower cathodic currents indicate a degradation of the electrode during oxygen evolution.

current can be tentatively attributed to a reduction of remaining small amounts of silver oxides. Surface layers of Ag_2O could have formed at potentials close to the equilibrium potential of silver oxide reduction (1173 mV vs. RHE). At higher overpotentials Ag_2O was fully consumed and the current was produced by the continuous reduction of oxygen alone. The porous structure of the GDE allowed good transport of reactants and caused a linear increase of current towards higher overpotentials. We did not observe a limiting current even at potentials as low as 100 mV. This demonstrates a good supply of oxygen to the active sites of the GDE. Thus, the peak performance of the electrode was not determined by mass or charge transport processes. The negligible contribution of a double layer current to the total current was confirmed by the collapsing lines of the forward and the backward scan. The facile kinetics showed an increase of ORR activity at elevated temperatures. A dashed line in Fig. 2 represents the repetition of the CV measurements after operating the electrode under oxygen evolution conditions. It shows the same features as for the fresh electrode. The lower current, however, is a clear indication for a degradation of the electrode during oxygen evolution. Possible degradation mechanisms are discussed below.

Cyclic voltammograms of the oxygen evolution are shown above 1.4 V in Fig. 2. At low overpotentials, we measured a small and constant anodic current. After a small dip, the current continuously increased towards higher potentials. A gap of around 0.01 A cm⁻² existed between the forward and the backward scan. At high currents the measurement signal showed significant noise. This coincided with the observation of gas bubble formation on the GDE surface [47]. These bubbles obstructed the transport of reactants in the porous electrode. The statistical process of bubble nucleation generated noise which could be seen in the current signal. Mechanical damage of the electrode was not observed. In the potential range studied, silver exhibits several oxidation states [48]. The small dips in the forward and backward scan arose from the corresponding changes in oxidation states. Some of these states are reported to dissolve in alkaline electrolytes [49,50]. The resulting changes in the surface morphology in turn led to a degradation of GDE performance. This could also have been an explanation for the gap between forward and backward scan. Another possible reason might have been a depletion of hydroxide ions in the liquid electrolyte due to transport limitations.

2.2.2. Electrochemical impedance spectroscopy

We report electrochemical impedance spectra (EIS) during oxygen reduction only. Under oxygen evolution conditions, the formation of gas bubbles heavily deteriorated the measurement signal. We used EIS to identify relevant physical processes at various polarizations. Impedance spectra were recorded in the frequency range from 100 mHz to 10 kHz. At each working point, the system was polarized for 5 min at a constant voltage before a sinusoidal excitation with an amplitude of 5 mV was imposed.

Fig. 3 shows Nyquist plots of impedance spectra at various polarizations in 1 M LiOH solution and at a temperature of 25 °C. The symbols represent data points from our measurements and the solid lines are the result of a fit to the equivalent circuit depicted in the inset of Fig. 5. The recorded spectra show features typical for porous electrodes [51]. The lowest impedance in the complex plane diagram corresponds to the highest frequency of the sinusoidal excitation. Towards lower frequencies the imaginary part linearly increased at an angle of approximately 45° with the real axis. Attached to this linear region we saw a depressed semi-circle. The radius of the semi-circle and thus the resistance of the electrode decreased at higher polarizations.

The resistance in the limit of infinite frequencies corresponded to the combined ohmic resistance of electrode and liquid electrolyte. The conductivity of silver, however, is very high and the contribution of the electrode to the resistance can be neglected [52]. If the signal of the excitation was not penetrating the whole pore space of the GDE [51], a linear increase of the imaginary part was observed. This feature typically appeared if the penetration depth λ was much smaller than the characteristic length scale of the pore network. In the present case the characteristic length was approximately given by the thickness of the electrode L_{GDE} . The penetration depth follows as [51]

$$\lambda = \sqrt{0.5rZ_{\text{elode}}\sigma_{\text{elyte}}} \quad (4)$$

Here Z_{elode} is the impedance of the electrode, r the mean pore diameter and σ_{elyte} the specific conductivity of the electrolyte solution.

At a frequency of 1 kHz λ is around 3 μm for the measurements shown in Fig. 3. The impedance of the electrode and the penetration depth increase [53] towards lower frequencies. At 1 Hz λ is already around 20 μm and the ac signal is able to penetrate the whole pore space. In this case, the impedance is comparable to one of a flat electrode and is represented by a deformed semi-circle in the complex plane diagram. The diameter of the semi-circle is representative of the charge transfer resistance of the ORR. This is

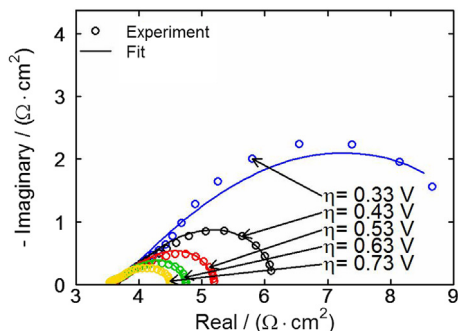


Fig. 3. Nyquist plot (100 mHz–10 kHz) of impedance spectra recorded in aqueous 1 M LiOH solution at a temperature of 25 °C. The corresponding Bode plot can be found in Fig. 7. Symbols represent experimental data and lines show results of the fit to the equivalent circuit model (see Fig. 5).

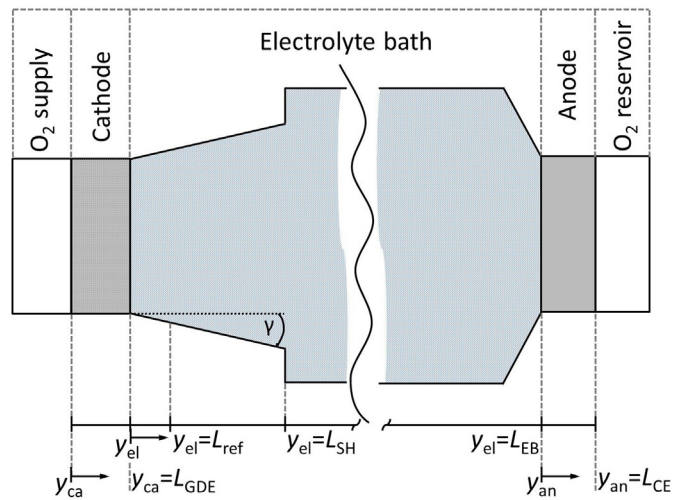


Fig. 4. Schematic depiction of the modeling domain. The geometry represents the experimental half-cell setup introduced in Section 2.1. In our 1D continuum model we consider a transport of reactants in cathode, electrolyte bath and anode. During discharge oxygen is consumed in the cathode (ORR) and released by the reverse reaction (OER) at the anode.

consistent with the observed decrease in kinetic resistance at higher polarizations.

3. Modeling

We use the electrochemical modeling software DENIS [19,54] for our numerical simulations outlined below. Originally developed for the simulation of fuel cells, we recently showed its ability to model Li–O₂ batteries. Our model for aqueous Li–O₂ batteries is described in detail in Ref. [33]. We will summarize it briefly, and discuss some modifications which are due to a different geometry. A list of symbols is given in Table 2, the constitutive equations of the model are provided in Table 3, and the kinetic mechanism is given in Table 4.

3.1. Model description

Fig. 4 schematically depicts the modeling domain describing the experimental setup (Section 2.1). In the 1D continuum model, the

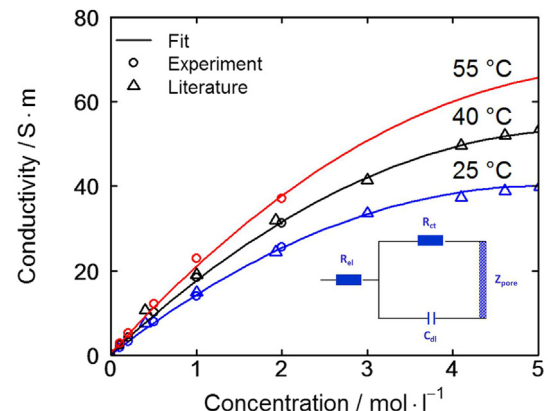


Fig. 5. Conductivity of electrolyte solution at various concentrations and temperatures. Open circles represent our experimental data as a result of the fit to the equivalent circuit (inset). Data from the literature (open triangles) [26] is shown for comparison. The solid line represents the best fit to the combined set of data (see Eq. (7)). Inset: Equivalent circuit model for porous electrodes [46]. The circuit consists of the electrolyte resistance R_{el} , the charge transfer resistance (R_{ct}) and double layer capacitance (C_{dl}). Z_{pore} represents a transmission line element [60].

Table 3

Summary of model equations [54,19] (cf. list of symbols for definition).

Process	Model equation	Nr.
<i>Gas-phase transport in porous electrodes</i>		
Species		
conservation	$\frac{\partial(c_{\text{gas}}^{\text{gas}} X_i)}{\partial t} = -\frac{\partial J_i^{\text{diff}}}{\partial y} - \frac{\partial J_i^{\text{conv}}}{\partial y} + \sum_m A_m^V \dot{s}_{i,m}$	(12)
Diffusive fluxes	$\frac{\partial(c_{\text{gas}}^{\text{gas}} X_i)}{\partial y} = -\sum_{j \in S_g} \frac{X_{ij}^{\text{diff}} - X_{j,i}^{\text{diff}}}{D_{ij}^{\text{eff}}}$	(13)
Convective fluxes	$J_i^{\text{conv}} = v_{\text{gas}} X_i c_{\text{gas}}$	(14)
Flow velocity	$v_{\text{gas}} = \frac{B_{\text{gas}}}{\eta_{\text{gas}}} \frac{\partial p_{\text{gas}}}{\partial y}$	(15)
Equation of state	$\rho_{\text{gas}} = \frac{p_{\text{gas}}}{RT} \bar{M}$	(16)
<i>Liquid-phase transport in porous electrodes</i>		
Species		
conservation	$\frac{\partial(\varepsilon c_i)}{\partial t} = -\frac{\partial(J_i^{\text{diff}})}{\partial y} - \frac{\partial(J_i^{\text{migr}})}{\partial y} - \frac{\partial(J_i^{\text{conv}})}{\partial y} + \sum_m A_m^V \dot{s}_{i,m}$	(17)
Diffusive fluxes	$J_i^{\text{diff}} = -D_i^{\text{diff,eff}} \frac{\partial c_i}{\partial y}$	(18)
Migrative fluxes	$J_i^{\text{migr}} = -D_i^{\text{migr,eff}} \frac{\partial \phi_{\text{elyte}}}{\partial y}$	(19)
Transport coefficients	$D_{\pm}^{\text{diff}} = D^0 + \frac{t_{\pm}}{z_{\pm} F} \frac{\sigma_D}{c_{\pm}} \text{ and } D_{\pm}^{\text{migr}} = \frac{t_{\pm}}{z_{\pm} F} \sigma$	(20)
Effective coefficients	$\chi^{\text{eff}} = \varepsilon_{\text{elyte}}^{\beta} \chi^0 = (s \varepsilon_0)^{\beta} \chi^0$	(21)
Convective fluxes	$J_i^{\text{conv}} = v_{\text{elyte}} c_i$	(22)
Flow velocity	$v_{\text{elyte}} = \frac{B_{\text{elyte}}}{\eta_{\text{elyte}}} \frac{\partial p_{\text{elyte}}}{\partial y}$	(23)
Equation of state	$\sum_i [\bar{V}_i + (p_{\text{elyte}} - p_0) \bar{r}_i] c_i = \varepsilon_{\text{elyte}}$	(24)
Charge conservation	$0 = \sum_i z_i F [J_i^{\text{diff}} + J_i^{\text{migr}} + J_i^{\text{conv}} + \sum_m (A_m^V \dot{s}_{i,m})]$	(25)
<i>Phase management in porous electrodes</i>		
Phase growth	$\frac{\partial \varepsilon_i}{\partial t} = \bar{M}_i \sum_m (A_m^V \dot{s}_{i,m})$	(26)
Volume restriction	$\sum_i \varepsilon_i (p_i) = 1$	(27)
<i>Current and voltage</i>		
Half cell voltage	$E = \phi_{\text{elde,ca}} - \phi_{\text{elyte,ref}}$	(28)
Potential step	$\Delta \Phi = \phi_{\text{elde}} - \phi_{\text{elyte}}$	(29)
Current density	$i = \int_{y=0}^{L_{\text{elde}}} (i_F + i_{\text{dl}}) dy$	(30)
Double layer current	$i_{\text{dl}} = A_{\text{dl}}^V c_{\text{dl}} \frac{\partial(\Delta \Phi)}{\partial t}$	(31)
Double layer capacity	$c_{\text{dl}} = \frac{\varepsilon (c_{\pm}, T) \varepsilon_0}{y_{\text{dl}}}$	(32)
Faraday current	$i_F = \sum_m (F A_m^V \dot{s}_{\text{electron},m})$	(33)
<i>Reactions and kinetics</i>		
Species		
source term	$\dot{s}_i = \nu_i \left(k_f \prod_{j \in R_i} a_j^{\nu_j} - k_r \prod_{j \in R_r} a_j^{\nu_r} \right)$	(34)
Forward rate constant	$k_f = k_f^0 \exp\left(-\frac{E_f^{\text{act}}}{RT}\right) \exp\left(-\frac{\beta z F}{RT} \Delta \Phi\right)$	(35)
Thermodynamic consistency	$\frac{k_f}{k_r} = \exp\left(-\frac{\Delta G}{RT}\right)$	(36)

time evolution of concentrations and potentials is determined based on conservation equations for mass and charge, respectively. We simulate CV and EIS measurements at various temperatures. The system is assumed to be isothermal during the measurements. During discharge pure oxygen gas enters the GDE at constant temperature and pressure and dissolves in the liquid electrolyte (Table 4, Eq. (37)). Dissolution is modeled as chemical reaction in our modeling approach (Table 3, Eqs. (34)–(36)). The kinetics of the dissolution reaction follow from the Hertz–Knudsen equation. We assume that 1% of the molecules hitting the gas–liquid interface are absorbed in the electrolyte [33]. Dissolved oxygen reacts with water and electrons forming hydroxide ions (Table 4, Eq. (38)). Transport in the gas phase and in the liquid phase is modeled by the Navier–Stokes equations (Table 3, Eqs. (12)–(15)) and concentrated solution theory (CST) (Table 3, Eqs. (17)–(23)), respectively [54,33]. We assume electroneutrality to determine the potential distribution in the liquid electrolyte (Table 3, Eq. (25)). The electronic resistivity of the GDE can be safely neglected due to the high conductivity of silver [52]. Effective transport coefficients in the liquid electrolyte are calculated via the Bruggeman correlation (Table 3, Eq. (21)).

$$\chi^{\text{eff}} = \varepsilon_{\text{elyte}}^{\beta} \chi^0 = (s \varepsilon_0)^{\beta} \chi^0,$$

where β is the so-called Bruggeman coefficient and $\varepsilon_{\text{elyte}}$ the volume fraction of the electrolyte. $\varepsilon_{\text{elyte}}$ can be calculated from the porosity of the electrode ε_0 and its saturation with liquid electrolyte s . The Bruggeman coefficient is a measure for the tortuosity of transport pathways in the porous structure. We assume that it is independent of the saturation and use the standard value 1.5 in our calculations. In the porous structure of the GDE, gas phase and liquid electrolyte are in mechanical equilibrium. The electrolyte saturation s is determined by the capillary pressure p_c which is defined as

$$p_c = \Delta p = p_{\text{gas}} - p_{\text{elyte}} = \sigma_{\text{elyte}} \sqrt{\frac{\varepsilon_0}{B_{\text{elyte}}}} J(s), \quad (5)$$

where p_{gas} and p_{elyte} are the pressures in the gas and liquid phase, respectively, σ_{elyte} is the surface tension of the electrolyte solution with respect to air [55,56], and B_{elyte} the permeability calculated from Kozeny–Carman equation [54,57]. We parameterize the phenomenological Leverett function $J(s)$ according to Hao et al. [41] (see Section 4.1). The pressure level in the liquid phase is determined by the hydrostatic pressure of the electrolyte bath. In our experiment, the liquid pressure is adjusted to meet the pressure of the gas phase ($\Delta p = 0$). The volume fractions of the gas and the liquid phase follow from their respective equations of state (Table 3, Eqs. (16) and (24)) [33]. In Ref. [33] we consider the precipitation of solid $\text{LiOH} \cdot \text{H}_2\text{O}$. In our experiments we keep the concentration of LiOH in the electrolyte bath well below the solubility limit. Thus, the formation of $\text{LiOH} \cdot \text{H}_2\text{O}$ is neglected in this study. At the counter electrode, we model the formation of oxygen via Eq. (40) (OER). The evolved oxygen is dissolved in the electrolyte and assumed to be in equilibrium with a surrounding O_2 atmosphere (Eq. (39)). We do not explicitly model the reference electrode in our approach. The electrolyte potential at the position of the reference electrode ($y_{\text{ref}} = 5 \text{ mm}$) directly constitutes the potential of a standard hydrogen electrode (SHE).

3.2. Simulation methodology

For the numerical simulation, all transport equations are discretized using a finite-volume (FV) approach in one dimension

Table 4

Summary of reactions in the different layers following Eq. (35).

Reaction	Equation	Nr.	Parameters	Value	Units
<i>Cathode</i>					
O ₂ solution	O ₂ ^(gas) ⇌ O ₂ ^(aq)	(37)	A ^V k ⁰ E _a A ^V k ⁰ E _a β	1·10 ⁴ 1.1·10 ² 0 3.3·10 ⁶ 9.6·10 ⁻⁴ 21.76 0.149	m ⁻¹ s ⁻¹ kJ mol ⁻¹ m ⁻¹ m ⁶ kmol ⁻² s ⁻¹ kJ mol ⁻¹ —
O ₂ reduction	O ₂ ^(aq) + 2H ₂ O + 4e ⁻ ⇌ 4OH ⁻	(38)			
<i>Anode</i>					
O ₂ dissolution	O ₂ ^(gas) ⇌ O ₂ ^(aq)	(39)	A ^V k ⁰ E _a A ^V k ⁰ E _a β	1·10 ² 1.1·10 ² 0 2·10 ⁴ 9.6·10 ⁻⁴ 21.76 0.149	m ⁻¹ s ⁻¹ kJ mol ⁻¹ m ⁻¹ m ⁶ kmol ⁻² s ⁻¹ kJ mol ⁻¹ —
O ₂ evolution	O ₂ ^(aq) + 2H ₂ O + 4e ⁻ ⇌ 4OH ⁻	(40)			

(denoted by y). We discretize the GDE with 30 non-uniform compartments. The smallest FV-compartments are located at the boundary to the electrolyte bath. Their width is chosen as 0.56 μm in order to resolve the penetration depth of the ac signal (Eq. (4)). The electrolyte bath itself is discretized with 10 equally-spaced FV-compartments. This coarse discretization is justified by small gradients in concentration and electrolyte potential in the bath. In our model we take into account the changes in the cross-sectional area A of the electrolyte bath (Fig. 4). The resulting equation for the conservation of the mass of species i in the liquid phase is

$$\frac{\partial(\epsilon c_i)}{\partial t} = \frac{1}{A} \frac{\partial}{\partial y} \left(A \left(J_i^{\text{diff}} + J_i^{\text{migr}} + J_i^{\text{conv}} \right) \right). \quad (6)$$

Modeling and simulation methodologies are implemented in the software DENIS [19,54]. We use the software package Cantera [58] for the calculation of (electro-) chemical source terms and the DAE solver LIMEX [59] for time-integration of the set of equations. Electrochemical impedance spectra are calculated by a step excitation of the reference electrode potential and numerical time integration of the current response [53]. The potential and current traces are Fourier transformed to obtain the impedance spectra in the frequency domain.

4. Results and discussion

In this section we discuss the results of measurements and simulations. First, we use the experimental data for the parameterization of the continuum model (Section 4.1). Model parameters, that is, the electrolyte conductivity, the kinetics of the ORR, the double layer capacitance, and the Leverett function, are determined in 1 M solution. We validate our model with CV and EIS measurements at various salt concentrations in Section 4.2. Note that we use a single set of parameters for all calculations.

Finally, in Section 4.3, we perform a sensitivity analysis of our continuum model to identify the most important parameters for electrode design.

4.1. Model parameterization

The model is parameterized based on data from our own experiments and from literature. Thermodynamic and transport parameters are taken from Ref. [33]. A list of geometric parameters of the setup and structural parameters of the GDE can be found in

Table 1. Chemical reactions and corresponding kinetic parameters are summarized in Table 4.

We use an equivalent circuit model for the analysis of the electrochemical impedance spectra (see Fig. 5). Equivalent circuit models are a viable and widely-used tool to identify physical processes and to extract physical parameters [60]. The elements of the equivalent circuit are adjusted to match the experimental data. The error in the fit is less than 3% for all measurements. This indicates a reasonable representation of physical processes. The circuit consists of the electrolyte resistance R_{el} in line with an RC element, representing the charge transfer resistance (R_{ct}) and double layer capacitance (C_{dl}) at the electrode-electrolyte interface. The porous electrode element Z_{pore} denotes a transmission line model, which reflects the porous structure of the GDE [60]. The elements of this equivalent circuit are described in detail in Ref. [46]. From the equivalent circuit model we extract the electrolyte conductivity and double layer capacitance. The experimental IV curves in turn are used to determine the kinetic parameters and the saturation of the GDE.

4.1.1. Electrolyte conductivity

The measured electrolyte conductivity is shown as function of temperature and LiOH concentration in Fig. 5. Our data is in good agreement with data from the literature also shown in Fig. 5 [26,61]. The solid line in Fig. 5 represents a fit to the combined set of data according to

$$\sigma_{\text{elyte}} = (-3.83584 + 0.01363T) + (-49.6837 + 0.2193T)c_{\text{LiOH}} + (1.54934 - 0.01038T)c_{\text{LiOH}}^2. \quad (7)$$

The fit agrees well with the experimental data at high concentrations. At low concentrations the conductivity increases strongly with increasing salt concentrations. Therefore, this region is afflicted with small uncertainties (Fig. 12).

4.1.2. Double layer capacitance

Upon characterization under transient conditions (CV, EIS), the electrical double layer at the electrode-electrolyte interface leads to additional capacitive currents. The roughness of the surface or slow adsorption of ions and chemical impurities on the surface can cause a dispersion of the capacitance. A constant phase element (CPE) can capture this dispersive behavior [51]. In our equivalent circuit we use a pure capacitive element and accept a minor decrease in fitting accuracy. Fig. 6 shows the double layer

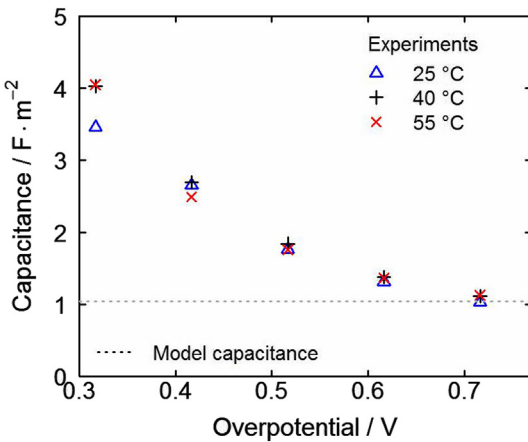


Fig. 6. Double layer capacitance in 1 M LiOH solution. Symbols represent the double layer capacitance from the fit to the equivalent circuit model at various polarizations. The dotted line represents the capacitance of the model and is included as a guide for the eye.

capacitance in 1 M LiOH solution at various polarizations. The capacitance decreases continuously and approaches a constant value at high overpotentials. The influence of temperature is less prominent in our measurements.

We model the electric double layer as an ideal parallel-plate capacitor. The area specific capacitance c_{dl} is given by

$$c_{dl} = \frac{\epsilon \epsilon^0}{y_{dl}}, \quad (8)$$

where ϵ is the dielectric constant of the solution, $\epsilon^0 = 8.85 \cdot 10^{-12} \text{ F m}^{-1}$ the permittivity of vacuum and y_{dl} the thickness of the double layer. In lack of experimental data for LiOH we use the dielectric constant for NaOH solution [62,63]. The capacitance at small overpotentials is very high and a polarization dependence of the capacitance alone does not explain the strong decrease of the fitted parameters. Most likely, the equivalent circuit fit includes ad- or desorption processes of ions on the electrode surface. Therefore, we neglect the potential dependence of c_{dl} and

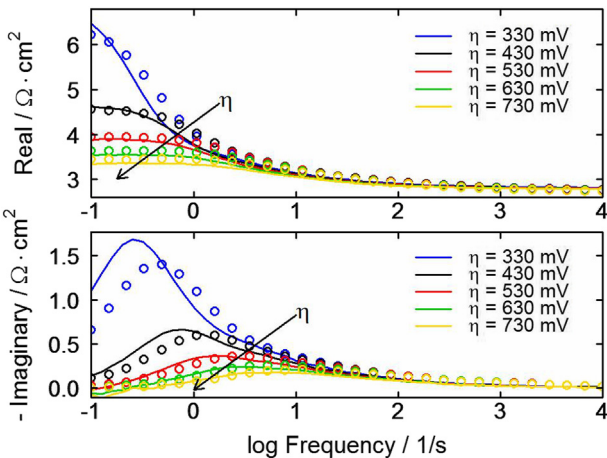


Fig. 7. Bode plots of impedance spectra in 1 M LiOH solution at 40 °C and various polarizations. Symbols represent the experimental data and solid lines show the results of the continuum simulations. The graph demonstrates the good agreement of our simulations with the experiments and validity of our model of the electric double layer.

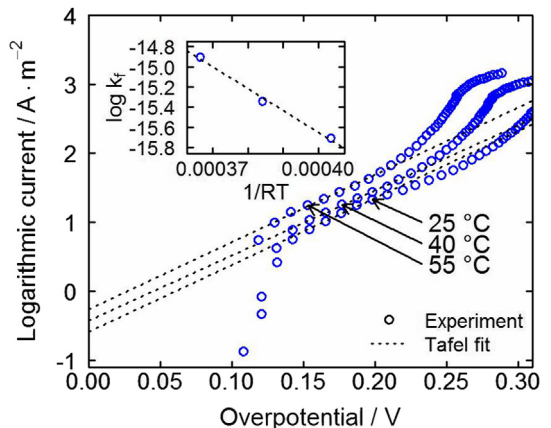


Fig. 8. Tafel analysis for the ORR in 1 M LiOH solution at temperatures of 25, 40 and 55 °C. Open circles show the experimental data of our CV measurements. The data is corrected for effects of mass transport. The dashed lines represent the best Tafel fit at overpotentials between $\eta_{eff} = 150 \text{ mV}$ and 200 mV . The inset shows the Arrhenius plot of the pre-exponential factors which were determined according to our kinetic model from the exchange current densities. All kinetic parameters are summarized in Table 4.

adjust y_{dl} to fit our experimental data at high polarization where the capacitance approaches a constant value. The capacitance of our model is shown as dotted line in Fig. 6. We use a double layer thickness y_{dl} of 5.0 Å, which approximately corresponds to two layers of molecular water [64] on the electrode surface. We justify our simplified description of the electrical double layer by comparing the relaxation times $\tau = R_{ct} c_{dl}$ of the charge transfer process. In a Bode plot, τ corresponds to the frequency at the maximum of the imaginary part. The position of the simulated maxima in Fig. 7 agrees fairly well with our experiments. We extrapolate c_{dl} to other salt concentrations by using the correlations for ϵ given in Refs. [62,63] in Eq. (8).

4.1.3. ORR kinetics

For the calculation of kinetic parameters we utilize the data from CV measurements in 1 M LiOH solution. We eliminate mass transport effects from the porous electrode by correcting the measured potential for corresponding overpotentials. The effective overpotential η_{eff} is

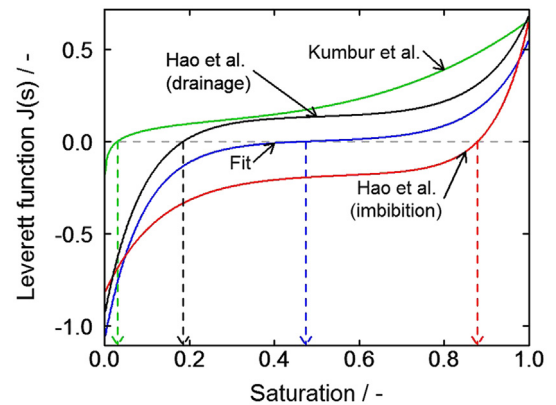


Fig. 9. Leverett function $J(s)$ as proposed by Kumbur et al. [39] (without MPL) and Hao et al. [41]. The correlations describe the relation between capillary pressure and saturation in porous media. Our fit is determined by adjusting an offset to the correlation of Hao et al. [41] to get a good agreement between simulated and measured IV curves (see Fig. 10).

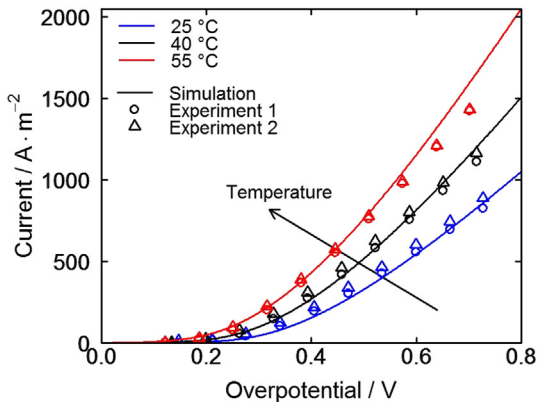


Fig. 10. IV curves in 1 M LiOH solution at various temperatures. The saturation of the GDE was adjusted to obtain a good agreement between experiments (symbols) and simulations (solid lines).

$$\eta_{\text{eff}} = \eta - R_{\text{tot}}i, \quad (9)$$

where $R_{\text{tot}} = R_{\text{el}} + Z_{\text{pore}}$ is the total mass transport resistance. R_{el} and Z_{pore} are determined from the equivalent circuit model. The Tafel plot with corrected overpotentials is shown in Fig. 8. A straight line is fitted to the Tafel regime between $\eta_{\text{eff}} = 150$ mV and 200 mV. The Tafel slope of ~ 100 mV decade $^{-1}$ gives a symmetry factor β_{Cathode} of ~ 0.15 [65]. We determine the exchange current densities for three different temperatures as the intercept of the Tafel line with the line of zero overpotential. For the calculation of rate constants, we assume a Butler–Volmer type global kinetic model (see Eq. (34)). The frequency factor and activation energy follow from the Arrhenius plot shown in the inset of Fig. 8. The kinetic parameters are summarized in Table 4. A short derivation of the parameters of the ORR can be found in the appendix.

4.1.4. Saturation of the GDE

In Ref. [33] we use the correlation of Kumbur et al. [39] for the calculation of GDE saturation. It was developed for the saturation of carbon cloth type GDLs in PEMFCs. The predicted saturations at $\Delta p = 0$ are very low. Wang et al. [66] point out that the saturation strongly depends on the structure of the medium. Therefore, we use the simplified expression of Hao et al. [41] (Fig. 9) and adjust the offset of the Leverett function $J(s)$ to fit our experimental IV curves in 1 M LiOH solution, as shown in Fig. 10. The resulting Leverett function is given by

$$J(s) = 1.34 \cdot 10^{-3} + 0.00498e^{9.404(s-0.5)} - 0.00397e^{-11.19(s-0.5)}. \quad (10)$$

This function gives a good agreement between simulated and experimental IV-curves over the complete investigated temperature and polarization range. The small deviation at high η is discussed in Section 4.2.1. Our model predicts a saturation of about $\sim 47\%$. This reflects the wetting behavior of water on Ag surfaces [67] and is slightly below the values previously used in the modeling of alkaline fuel cells [68,69].

4.2. Model validation

The model as outlined above is used to simulate the electrochemical measurements described in Section 2.2. We focus here on the oxygen reduction regime because of electrode degradation and a noisy signal during oxygen evolution. Liquid-phase transport

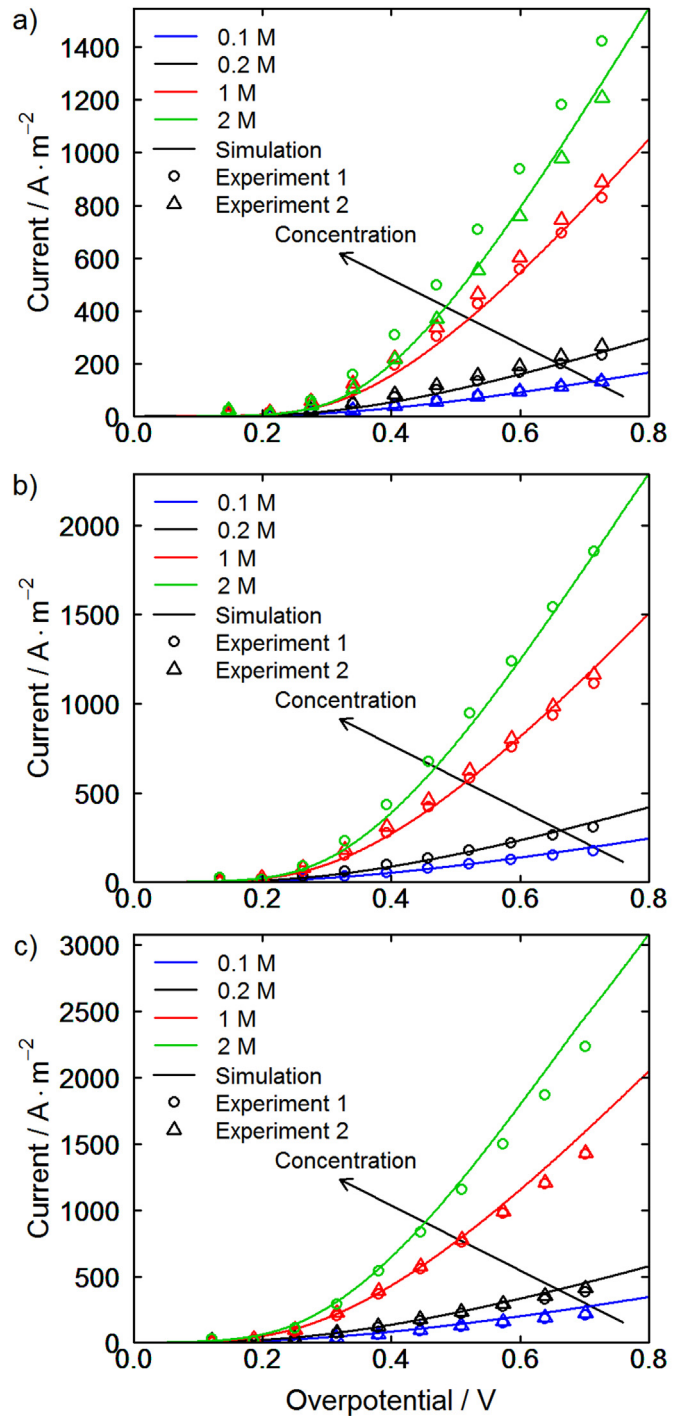


Fig. 11. IV curves in aqueous LiOH solution. The concentration of electrolyte solution was varied between 0.1 and 2 M. Graphs a)–c) show a comparison between simulation (solid lines) and experiment (symbols) at 25, 40 and 55 °C, respectively.

processes during oxygen reduction and oxygen evolution are expected to be similar.

In the following Sections we validate our model separately for IV curves and impedance spectra. For both techniques our simulations agree very well with the experiments over a wide range of concentrations, temperatures and overpotentials.

4.2.1. Cyclic voltammetry

We simulate a potential sweep at a scan rate of 1 mV s $^{-1}$, like in our experiments. Both experiments and model show a stationary

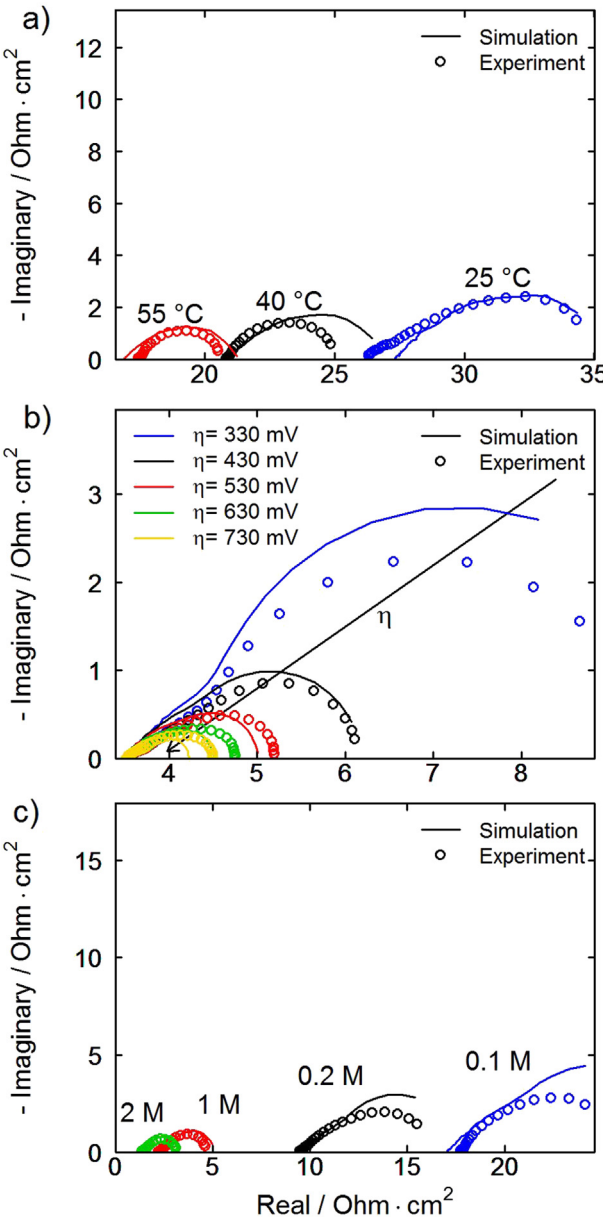


Fig. 12. Impedance spectra of the Ag electrode in the complex plane at various conditions. Symbols represent the experimental data and solid lines are the results of the impedance simulations of our continuum model. a) Spectra in 0.1 M solution and a polarization of 700 mV vs. RHE. b) Series of spectra at various overpotentials in 1 M solution and at a temperature of 25 °C. c) Spectra at 40 °C and a polarization of 900 mV vs. RHE.

behavior at these low scan rates, therefore, results are presented as IV curves. In Fig. 11 we compare IV curves of measurements and simulations for various temperatures. As explained in the previous Section 4.1.4, we adjust the saturation dependence $J(s)$ to give a good fit in 1 M LiOH solution. The good quantitative agreement with the experimental data at other concentrations proves the validity of our model.

The model slightly overpredicts current densities at high overpotentials as already seen in Section 4.1.4. This indicates that relevant rate-limiting processes at high overpotentials and currents are not fully represented in the current model. Pinnow et al. [44] report a change in the apparent Tafel slope of their experiments on silver GDEs in NaOH solution. They explain it with a possible change in

the adsorption isotherm of reaction intermediates and use a second Tafel slope at high overpotentials. Similar observations for Pt catalysts in alkaline media [70,71] support this assumption. In the present model we use one single-step charge-transfer reaction to describe the kinetics at all concentrations, temperatures and overpotentials. A more rigorous elementary kinetic description of the ORR could give some additional insights on this topic [27,72,73]. However, such a detailed treatment of kinetics is out of the scope of this work on transport phenomena of porous electrodes. Similar changes in the slope of the IV curve are also reported for PEMFCs [74,75]. This effect is attributed to a limited supply of O_2 through a thin film of ionomer on the electrode surface. The nature of this additional transport resistance is not yet fully understood and subject of ongoing research. Suzuki et al. show that the dissolution of O_2 in the ionomer might be the rate limiting step [75]. However, we could not confirm this observation for our aqueous system (see Section 4.3.1).

In the case of a limiting transport of O_2 , we would expect smaller deviations of the IV curves at low concentrations. The solubility and diffusivity of O_2 is high at low salt concentrations in the electrolyte [76,77,33]. Still, we observe the same discrepancy to our experiments. In the literature, flooded agglomerate models are suggested to include the transport of O_2 in the agglomerate and electrolyte film [44,75]. This requires an additional parameterization of the model with unknown structural quantities of the agglomerate. For the sake of simplicity and in order to avoid "over-parameterization" we do not pursue this approach here.

4.2.2. Electrochemical impedance spectroscopy

Impedance spectra from simulation and experiment are shown in Fig. 12 for various conditions. Overall, simulations and experiment are in a good qualitative agreement. We again stress that we use only one set of physical parameters for our simulations for all experimental conditions. This is an important difference to equivalent circuit models, where each spectrum is fitted individually. Our continuum model reproduces the characteristic shape of impedance spectra of porous electrodes in the complex plane. Its features are described in detail in Section 2.2.2. The intersection with the real-axis is in good agreement for experiments and simulations at high concentrations. At lower concentrations we see minor deviations of our simulated data. We attribute this to a lower accuracy of the fit of ionic conductivity in this region (see Section 4.1.1). At lower frequencies we observe a depressed semi-circle closing into a straight line with a slope of 45°, originating from transport and reaction in the porous electrode. The diameter of the semi-circle corresponds to the resistance of the ORR. At low temperatures and η the model overpredicts the experiments, whereas at high temperatures and η experiments are underpredicted. This discrepancy is consistent with the trends observed for IV curves (Section 4.2.1). Deviations at high temperatures and η are probably due to additional transport resistances or changes in the reaction mechanism of the ORR which we do not capture in our simplified 1D model. The increased resistance at low temperatures and η is due to our fitting procedure as we adjust $J(s)$ to get a good agreement at higher currents (see Section 4.1.4).

4.3. Discussion of parameters

We next perform a sensitivity analysis of the validated continuum model in order to identify the most important physico-chemical processes. The relative sensitivity s_ζ of the current density i on the change of parameter ζ is given by

$$s_\zeta = \frac{(i - i^0)/i^0}{(\zeta - \zeta^0)/\zeta^0}. \quad (11)$$

The parameters are varied individually by 5% of their original value (indicated by superscript 0). We perform the sensitivity analysis at 300, 500 and 700 mV overpotential. A sensitivity close to zero indicates parameters with only a small impact, whereas a high sensitivity reveals a limiting influence on the system performance. A sensitivity of unity means direct proportionality between the varied parameter and the current.

Results of the sensitivity analysis in 1 M LiOH at 25 °C are shown in Fig. 13. The parameters are grouped according to their effect on physical processes. The first part shows kinetic parameters, the second part transport parameters and the third part geometrical parameters. In the following discussion we put an emphasis on the structural parameters, which are important design parameters for the future development of GDEs.

4.3.1. Kinetic parameters

The kinetic parameters of the GDE show the highest impact on the system performance. This highlights the need for the development of novel catalysts [47,78–80]. Especially the symmetry factor of the ORR exhibits the highest sensitivity of all parameters. The kinetic parameters of the anode show a negligible sensitivity. This is expected in the simulated three-electrode setup and confirms our model of the counter electrode (Section 3.1). The dynamics of the O₂ dissolution at the cathode are represented by the rate constant of the reaction $k_{O_2}^0$. Even at high overpotentials and currents we do not see a limiting effect of the

O₂ dissolution in our model based on the Hertz–Knudsen equation (see Section 4.2.1).

4.3.2. Transport parameters

The sensitivity of transport parameters is comparatively small. Even at high overpotentials the diffusion coefficients of LiOH and O₂ in the liquid phase show only a small influence on the performance. Particularly, the impact of D_{O_2} is negligible. This is due to the excellent transport of O₂ in the gas phase of the GDE. Additionally, we neglect the transport resistance in the electrolyte film on the electrode surface. Thus, a slightly higher influence can be expected for the 3D system (see Section 4.2.1). Similarly, the sensitivity of the transference number t_\pm and the diffusion coefficient of LiOH D_{LiOH} are quite small. This can be attributed to the high ionic conductivity of the aqueous electrolyte. However, these parameters are very important during deep discharge of the battery as they determine the local precipitation of solid LiOH·H₂O. The low sensitivity of these transport parameters is beneficial for the accuracy of our model. They are calculated based on several assumptions from the literature [33]. An exception is the ionic conductivity of the electrolyte σ_{elyte} . Its significance is due to the comparatively large electrolyte region between the GDE and the reference electrode. Here, a large drop in the electrolyte potential occurs. This decreases the potential step $\Delta\phi$ which drives the electrochemical reaction in the GDE. In a real battery this distance is much smaller. Still the importance of this parameter for the transport of ions will be significant.

4.3.3. Structural parameters

The structure of the GDE shows a high influence on the system performance. Porosity ε_0 and tortuosity τ are important parameters for the transport of reactants (see Eq. (21)). In the present model, the tortuosity is determined by the Bruggeman coefficient β (Eq. (21)). High porosities improve the supply of reactants to the active sites on the electrode surface. In contrast, a high Bruggeman coefficient decreases the effective transport properties and causes the negative sign of the sensitivities. The specific surface areas at the cathode $A_{Cathode}^V$ and anode A_{Anode}^V are multiplicative factors in the rate expression of the electrochemical source term (Eq. (17)). Thus, their sensitivity is the same as $k_{Cathode}^0$ and k_{Anode}^0 , respectively.

The thickness of the electrode is an important parameter regarding the power density of the GDE. The sensitivity strongly depends on the applied overpotential. Fig. 14a shows the local Faradaic current along the y direction of the GDE. At low overpotentials the ORR proceeds in the whole GDE at almost the same rate. At high overpotentials the local current shows a considerable gradient, strongly increasing from the gas inlet towards the porous electrode/electrolyte bath interface. The gradient is caused by the ohmic resistance of the electrolyte. It is enhanced by a gradient of dissolved O₂ as shown in Fig. 14b (solid lines, discussed below). If the gradient in the local Faradaic current is small, a change in thickness causes a higher sensitivity compared to sensitivities at higher gradients.

The open symbols in Fig. 14b represent the solubility of O₂ (i.e., the concentration in the limit of thermodynamic equilibrium). The solubility of O₂ depends on the local concentration of LiOH. This effect is known as salting-out [76,77]. During oxygen reduction the local concentration of LiOH in the electrode increases in an inhomogeneous way such that higher concentrations are present close to the porous electrode/electrolyte bath interface. Fig. 14 shows that for all overpotentials, the simulated concentration (which includes transport limitations and salting-out) is very close to the solubility (which includes only salting-out). Thus, the decrease in O₂ concentration towards the electrolyte ($y_{ca} = L_{GDE}$)

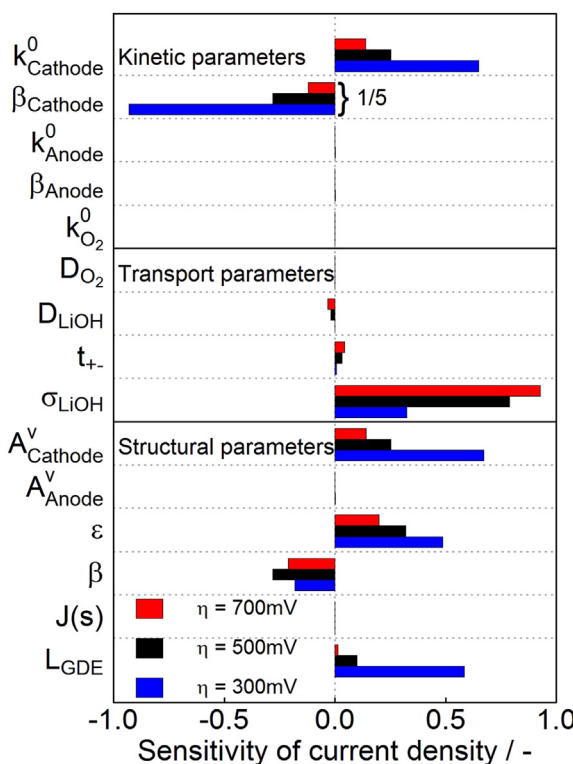


Fig. 13. Sensitivity analysis (Eq. (11)) at 300, 500, and 700 mV overpotential. Upper part: kinetic parameters, middle part: transport parameters, bottom part: geometrical parameters. The sensitivity of $\beta_{Cathode}$ is divided by 5 for convenience.

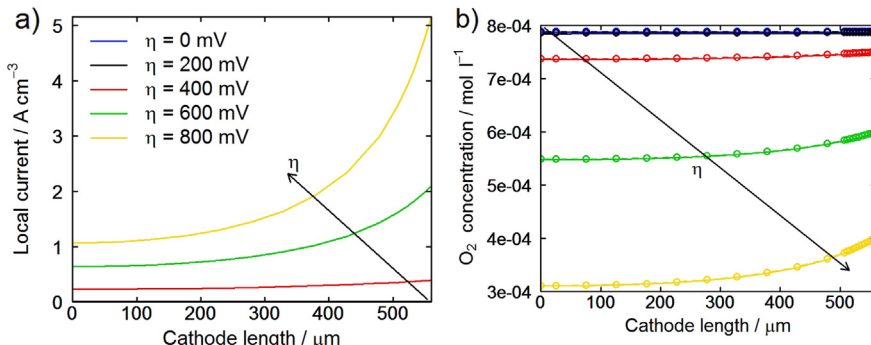


Fig. 14. Spatial profiles of Faradaic current a) and concentration of dissolved O_2 b) in the cathode at various overpotentials. Simulations are run at a temperature of 25 °C and a LiOH concentration of 1 M. Symbols in graph b) indicate the O_2 concentration in thermodynamic equilibrium. The gas inlet is at $y = 0$, the electrolyte bath at $y = 560 \mu m$.

is only due to salting-out and not due to a mass transport limitation of O_2 . This demonstrates the good supply of O_2 even at high overpotentials.

The sensitivity of the saturation is represented in the form of the Leverett function $J(s)$. Although the sensitivity is small in the studied parameter range close to 0.47, the saturation is crucial for the transport of reactants. In Fig. 15 we compare the performance of the system for several Leverett functions from the literature (see Fig. 9). In the correlations of Kumbur et al. [39] we neglect the contribution of the micro-porous layer (MPL). The other correlations are taken from Hao et al. [41] and are the basis for our own fit to the experimental data. Note that the predicted saturations range from 0.05 (Kumbur et al.) to 0.88 (Hao et al. for imbibition).

The Leverett function of Hao et al. for imbibition gives the highest saturation and the simulated electrode shows the best performance in terms of current density. The IV curves of other $J(s)$ are shifted towards higher overpotentials, i.e., the resulting current density is lower. The reason is a slower transport of reactants which is due to smaller effective transport coefficients in the liquid electrolyte (see Eq. (21)). Thus, a large part of the overpotential is needed to sustain the transport of reactants and less can be used to drive the electrochemical reaction. This study clearly shows the importance of the saturation on the system performance. Further investigations, experimentally as well as theoretically, are needed for a better description of two-phase flow in the porous structure of the GDE.

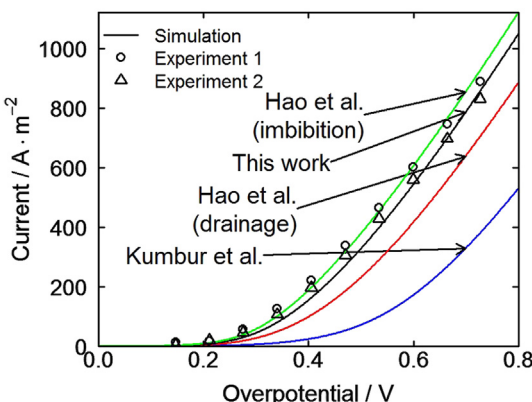


Fig. 15. Simulated IV curves for different correlations of the Leverett function from the literature [41,39]. Resulting saturations span from 0.05 (Kumbur et al.) up to 0.88 (Hao et al. for imbibition).

5. Conclusions

Aqueous Li– O_2 batteries are interesting candidates for mobile applications due to their high theoretical energy density. We have presented a combined modeling and experimental study of the performance and properties of an Ag/Ag₂O gas diffusion electrode (GDE) in aqueous lithium hydroxide solutions for the use in Li– O_2 batteries.

In the first part of this work, we discussed results of half-cell measurements for ORR and OER. We performed cyclic voltammetry and electrochemical impedance spectroscopy at various LiOH concentrations (0.1–2 mol l⁻¹), temperatures (298.15–328.15 K), and polarizations (500–1100 and 1400–1950 mV vs. RHE). The electrode showed high performance in the ORR regime. The transport of oxygen through the gas phase was found to be fast and not rate limiting. In the OER regime, we observed degradation of the electrode. The measurements provide an excellent basis for subsequent parameterization and validation of a 1D continuum model.

In the second part of this work, we presented a physico-chemical model of the half-cell experiments. The model accounts for the dissolution and reduction of oxygen in the electrolyte, as well as for the two-phase transport of gas-phase oxygen, liquid phase, and dissolved ions in the porous electrode. All parameters stem either from our own experiments or the extensive literature on aqueous electrolytes.

The results of our simulations agree favorably with the experiments over the whole temperature and concentration range studied. Our model reproduces the characteristic shapes of impedance spectra and IV curves. At high overpotentials, however, small deviations in IV curves and impedance spectra were observed, probably due to a change in reaction mechanism or additional transport resistances.

Continuum modeling contributes to gaining a fundamental understanding of relevant physico-chemical processes in the electrode and allows a systematic development of the electrode performance. To this aim, we have identified critical parameters via sensitivity analysis of the validated model. The ORR reaction kinetics were shown to have the biggest impact on the electrode performance. This highlights the need for further development of highly efficient catalysts. Also the electrode micro-structure, which determines the transport of reactants to the active surfaces, influences the battery performance. In this respect, the saturation of the GDE pores with liquid electrolyte is very important. Detailed investigations of this issue have been carried out both experimentally [35–40] and theoretically [41,81,82] in the context of PEM fuel cells. In the present study, the wetting behavior of the Ag-GDE is not known precisely. A closer determination of the electrolyte saturation in the GDE is subject of work in progress.

Table 2
List of symbols.

Symbol	Unit	Meaning	Eq.
A	—	Cross-sectional area perpendicular to y direction	(21)
A_m^V	$\text{m}^2 \text{m}^{-3}$	Volume-specific surface area	(12)
B_j	m^2	Permeability of the porous electrode	(15) and (23)
C_i	mol m^{-3}	Concentration of species i in a bulk phase	(17)
C_{dl}	F m^2	Area-specific double layer capacitance	(31)
D_i^{eff}	$\text{m}^2 \text{s}^{-1}$	Effective diffusion coefficient of species i	(21)
D_i^{migr}	$\text{m}^2 \text{s}^{-1}$	Effective migration coefficient of species i	(21)
E	E	Cell/half-cell voltage	(28)
E_f^{act}	J mol^{-1}	Activation energy of forward and reverse reactions	(35)
F	C mol^{-1}	Faraday constant	(25)
i	—	Index of species or phases	(12)
i	A m^{-2}	Current density	(30)
i_F	A m^{-3}	Faradaic current density	(33)
i_{dl}	A m^{-3}	Current density from electric double layer	(31)
j	—	Index of species or phases	(18) and (19)
J_i	$\text{mol m}^{-2} \text{s}^{-1}$	Flux of species i	(14)
k_f, k_r	—	Forward and backward rate constant	(36)
k^0	—	Pre-exponential factor in Arrhenius equation	(35)
m	—	Index of chemical reactions and interfaces	(12)
M_i	kg mol^{-1}	Molar mass of species i	(16)
\bar{M}_j	kg mol^{-1}	Mean molar mass of phase j	(16)
p_j	Pa	Pressure	(15)
r	m	Pore radius	(4)
R	$\text{J K}^{-1} \text{mol}^{-1}$	Ideal gas constant	(16)
R	Ωcm^2	Ohmic resistance	—
s	—	Saturation of porous electrode	(21)
\dot{s}_i	$\text{mol m}^{-2} \text{s}^{-1}$	Chemical production rate of species/phase i	(34)
t	s	Time	(12)
t_{\pm}	—	Transference number	(20)
T	K	Temperature	(16)
\bar{V}_i	$\text{m}^3 \text{mol}^{-1}$	Partial molar volume	(24)
X_i	—	Mole fraction of species i	(13)
y	m	Spatial position through thickness	(12)
z	—	Number of electrons transferred in charge-transfer step	(35)
z_i	—	Charge of species i	(20)
Z	$\text{m}\Omega \text{cm}^2$	Impedance	(4)
β_m	—	Symmetry factor of charge transfer reaction	(35)
β	—	Bruggeman coefficient	(21)
$\Delta\Phi$	V	Electric potential difference	(29)
ΔG	J mol^{-1}	Gibbs free energy of the reaction	(36)
ϵ	—	Relative permittivity	(8)
ϵ^0	F m^{-1}	Permittivity of vacuum	(8)
ϵ_i	—	Volume fraction of phase i	(12)
ϵ_0	—	Porosity	(21)
$\bar{\kappa}_i$	$\text{m}^3 \text{mol}^{-1} \text{Pa}^{-1}$	Partial molar compressibility	(24)
λ	m	Penetration depth of AC signal	(4)
η	V	Overpotential	(9)
η_j	$\text{kg m}^{-1} \text{s}^{-1}$	Viscosity	(23)
ν_i	—	Stoichiometric coefficient of species i	(34)
ϕ_j	V	Electric or ionic potential	(19)
ρ_j	kg m^{-3}	Density	(16)
σ	S m	Ionic or electronic conductivity	(20)
χ	—	Variable for effective transport properties	(21)
ζ	—	Parameters in the sensitivity analysis	(11)

Acknowledgments

Financial support from the German Ministry of Education and Research (BMBF) in the framework of the LuLi project (03X4624B) is gratefully acknowledged.

Appendix A. Derivation of kinetic parameters

Reaction equations in our framework [54,19,58] follow the law of mass action kinetics according to

$$\dot{s}_i = \nu_i \left(k_f \prod_{j \in R_f} a_j^{\nu'_j} - k_r \prod_{j \in R_r} a_j^{\nu''_j} \right) \quad (\text{A.1})$$

where k_f is given in Arrhenius form as function of temperature and the potential step at the electrode–electrolyte interface

$$k_f = \tilde{k}_f(T) \exp\left(-\frac{\beta z F}{RT} \Delta\Phi\right) = k_f^0 \exp\left(-\frac{E_f^{\text{act}}}{RT}\right) \exp\left(-\frac{\beta z F}{RT} \Delta\Phi\right). \quad (\text{A.2})$$

The Faradaic current i_F results as the sum of all charge-transfer reactions

$$i_F = \sum_m \left(F A_m^V \dot{s}_{\text{electron},m} \right). \quad (\text{A.3})$$

In the present case the only reaction contributing to the Faradaic current is the oxygen reduction reaction



The equation for the Faradaic current follows from Eqs. (A.1)–(A.3) as

$$i_F = 4F \left(\tilde{k}_F(T) c_{O_2} c_{H_2O}^2 \exp\left(-\frac{\beta zF}{RT} \Delta\Phi\right) - \tilde{k}_F(T) c_{OH^-}^4 \exp\left(\frac{(1-\beta)zF}{RT} \Delta\Phi\right) \right) \quad (A.5)$$

In the limit of high overpotentials (Tafel analysis) we can neglect the backmost part of Eq. (A.5).

$$i_F = 4F \tilde{k}_F(T) c_{O_2} c_{H_2O}^2 \exp\left(-\frac{\beta zF}{RT} \Delta\Phi\right) \quad (A.6)$$

We define the exchange current density i_0 by

$$i_0 = 4F \tilde{k}_F(T) c_{O_2} c_{H_2O}^2. \quad (A.7)$$

By inserting i_0 in Eq. (A.6) we get the well-known form of the Tafel equation

$$i_F = i_0 \exp\left(-\frac{\beta zF}{RT} \Delta\Phi\right). \quad (A.8)$$

A Tafel analysis yields the parameters i_0 and β at each temperature. We calculate $\tilde{k}_F(T)$ from Eq. (A.7) and determine the pre-exponential factor k_F^0 and the activation energy of the reaction from the Arrhenius plot shown in the inset of Fig. 8. For our simulations we use a temperature average value of β .

References

- [1] B. Scrosati, J. Garche, *J. Power Sources* 195 (2010) 2419–2430.
- [2] A. Kraytsberg, Y. Ein-Eli, *Adv. Energy Mater.* 2 (2012) 922–939.
- [3] P.G. Bruce, S.A. Freunberger, L.J. Hardwick, J.-M. Tarascon, *Nat. Mater.* 11 (2012) 19–29.
- [4] G. Girishkumar, B. McCloskey, A.C. Luntz, S. Swanson, W. Wilcke, *J. Phys. Chem. Lett.* 1 (2010) 2193–2203.
- [5] J. Christensen, P. Albertus, R.S. Sanchez-Carrera, T. Lohmann, B. Kozinsky, R. Liedtke, J. Ahmed, A. Kojic, *J. Electrochem. Soc.* 159 (2012) R1–R30.
- [6] A. Kraytsberg, Y. Ein-Eli, *J. Power Sources* 196 (2010) 886–893.
- [7] Y.-C. Lu, B.M. Gallant, D.G. Kwabi, J.R. Harding, R.R. Mitchell, M.S. Whittingham, Y. Shao-Horn, *Energy Environ. Sci.* 6 (2013) 750–768.
- [8] M. Park, H. Sun, H. Lee, J. Lee, J. Cho, *Adv. Energy Mater.* 2 (2012) 780–800.
- [9] K.F. Blurton, A.F. Sammells, *J. Power Sources* 4 (1979) 263–279.
- [10] K.M. Abraham, Z. Jiang, *J. Electrochem. Soc.* 143 (1996) 1–5.
- [11] S.P. Ong, Y. Mo, G. Ceder, *Phys. Rev. B* 85 (2012) 081105.
- [12] J.S. Hummelshoj, J. Blomqvist, S. Datta, T. Vegge, J. Rossmeisl, K.S. Thygesen, A.C. Luntz, K.W. Jacobsen, J.K. Norskov, *J. Chem. Phys.* 132 (2010) 071101.
- [13] V. Viswanathan, K.S. Thygesen, J.S. Hummelshoj, J.K. Norskov, G. Girishkumar, B.D. McCloskey, A.C. Luntz, *J. Chem. Phys.* 135 (2011) 214704.
- [14] P. Albertus, G. Girishkumar, B. McCloskey, R.S. Sanchez-Carrera, B. Kozinsky, J. Christensen, A.C. Luntz, *J. Electrochem. Soc.* 158 (2011) A343–A351.
- [15] B. Horstmann, B. Gallant, R. Mitchell, W.G. Bessler, Y. Shao-Horn, M.Z. Bazant, *J. Phys. Chem. Lett.* 4 (2013) 4217–4222.
- [16] S.S. Sandhu, G.W. Brutchen, J.P. Fellner, *J. Power Sources* 170 (2007) 196–209.
- [17] R.E. Williford, J.-G. Zhang, *J. Power Sources* 194 (2009) 1164–1170.
- [18] P. Andrei, J.P. Zheng, M. Hendrickson, E.J. Plichta, *J. Electrochem. Soc.* 157 (2010) A1287–A1295.
- [19] J.P. Neidhardt, D.N. Fronczek, T. Jahnke, T. Danner, B. Horstmann, W.G. Bessler, *J. Electrochem. Soc.* 159 (2012) A1528–A1542.
- [20] S.A. Freunberger, Y.H. Chen, Z.Q. Peng, J.M. Griffin, L.J. Hardwick, F. Barde, P. Novak, P.G. Bruce, *J. Am. Chem. Soc.* 133 (2011) 8040–8047.
- [21] B.D. McCloskey, D.S. Bethune, R.M. Shelby, G. Girishkumar, A.C. Luntz, *J. Phys. Chem. Lett.* 2 (2011) 1161–1166.
- [22] R. Black, B. Adams, L.F. Nazar, *Adv. Energy Mater.* 2 (2012) 801–815.
- [23] Z. Peng, S.A. Freunberger, Y. Chen, P.G. Bruce, *Science* 337 (2012) 563–566.
- [24] M.J. Trahan, S. Mukerjee, E.J. Plichta, M.A. Hendrickson, K.M. Abraham, *J. Electrochem. Soc.* 160 (2013) A259–A267.
- [25] T. Zhang, N. Imanishi, Y. Takeda, O. Yamamoto, *Chem. Lett.* 40 (2011) 668–673.
- [26] P.J. Gierszewski, P.A. Finn, D.W. Kirk, *Fusion Eng. Des.* 13 (1990) 59–71.
- [27] J.S. Spendelow, A. Wieckowski, *Phys. Chem. Chem. Phys.* 9 (2007) 2654–2675.
- [28] Y. Shimonishi, T. Zhang, N. Imanishi, D. Im, D.J. Lee, A. Hirano, Y. Takeda, O. Yamamoto, N. Sammes, *J. Power Sources* 196 (2011) 5128–5132.
- [29] S. Visco, E. Nimon, B. Katz, *Honolulu PRiME, ECS*, 2012, p. 1156.
- [30] O.Y.N. Imanishi, Y. Takeda, *Electrochemistry* 80 (2012) 706–715.
- [31] J. Wolfenstine, *J. Mater. Sci.* 45 (2010) 3954–3956.
- [32] P. Stevens, G. Toussaint, G. Caillon, P. Viaud, P. Vinatier, C. Cantau, O. Fichet, C. Sarrasin, M. Mallouki, *ECS Trans.* 28 (2010) 1–12.
- [33] B. Horstmann, T. Danner, W.G. Bessler, *Energy Environ. Sci.* 6 (2013) 1299–1314.
- [34] F. Bidault, D.J.L. Brett, P.H. Middleton, N.P. Brandon, *J. Power Sources* 187 (2009) 39–48.
- [35] J.T. Gostick, M.W. Fowler, M.A. Ioannidis, M.D. Pritzker, Y. Volkovich, A. Sakars, *J. Power Sources* 156 (2006) 375–387.
- [36] T.V. Nguyen, G. Lin, H. Ohn, X. Wang, *Electrochim. Solid-State Lett.* 11 (2008) B127–B131.
- [37] E.C. Kumbur, K.V. Sharp, M.M. Mench, *J. Electrochem. Soc.* 154 (2007) B1295–B1304.
- [38] E.C. Kumbur, K.V. Sharp, M.M. Mench, *J. Electrochem. Soc.* 154 (2007) B1305–B1314.
- [39] E.C. Kumbur, K.V. Sharp, M.M. Mench, *J. Electrochem. Soc.* 154 (2007) B1315–B1324.
- [40] S. Dwenger, G. Eigenberger, U. Nieken, *Transp. Porous Med.* 91 (2011) 281–294.
- [41] L. Hao, P. Cheng, *Int. J. Heat Mass Tranfer* 55 (2012) 133–139.
- [42] S. Srinivasan, H. Hurwitz, *Electrochim. Acta* 12 (1967) 495–512.
- [43] J. Giner, C. Hunter, *J. Electrochem. Soc.* 116 (1969) 1124.
- [44] S. Pinnow, N. Chavan, T. Turek, *J. Appl. Electrochem.* 1053 (2011) 1–12.
- [45] A. Bulan, A Process for Producing Gas Diffusion Electrodes, DE Patent App. DE102005023615A1, 2006.
- [46] N. Wagner, M. Schulze, E. Gölzow, *J. Power Sources* 127 (2004) 264–272.
- [47] D. Wittemaier, T. Danner, N. Wagner, K.A. Friedrich, *J. Appl. Electrochem.* 44 (2013) 73–85.
- [48] S.S. Abd El Rehim, H.H. Hassan, M.A.M. Ibrahim, M.A. Amin, *Monatsh. Chem.* 129 (1998) 1103–1117.
- [49] V. Maurice, L.H. Klein, H.-H. Strehblow, P. Marcus, *J. Phys. Chem. C* 111 (2007) 16351–16361.
- [50] E.R. Savinova, B. Pettinger, K. Doblhofer, *J. Electroanal. Chem.* 430 (1997) 47–56.
- [51] A. Lasia, in: B.E. Conway, J. Bockris, R. White (Eds.), *Modern Aspects of Electrochemistry*, vol. 32, Kluwer Academic/Plenum Publishers, New York, 1999, pp. 143–248.
- [52] R.A. Matula, *J. Phys. Chem. Ref. Data* 8 (1979) 1147.
- [53] S. Gewies, W.G. Bessler, *J. Electrochim. Soc.* 155 (2008) B937–B952.
- [54] W.G. Bessler, S. Gewies, M. Vogler, *Electrochim. Acta* 53 (2007) 1782–1800.
- [55] N. Vargaftik, B. Volkov, L. Voljak, *J. Phys. Chem. Ref. Data* 12 (1983) 817–820.
- [56] V.S. Markin, A.G. Volkov, *J. Phys. Chem. B* 106 (2002) 11810–11817.
- [57] J. Bear, *Dynamics of Fluids in Porous Media*, first ed., Elsevier, New York, 1972.
- [58] D.G. Goodwin, Cantera, 2012, <http://code.google.com/p/cantera>.
- [59] P. Deufhard, E. Hairer, J. Zugck, *Numer. Math.* 51 (1987) 501–516.
- [60] N. Wagner, in: E. Barsoukov, J. Macdonald (Eds.), *Impedance Spectroscopy: Theory, Experiment, and Applications*, second ed., John Wiley&Sons, Inc., 2005, pp. 497–537.
- [61] T.S. Light, S. Licht, A.C. Bevilacqua, K.R. Morash, *Electrochim. Solid-State Lett.* 8 (2005) E16–E19.
- [62] R. Buchner, G. Hefter, P.M. May, P. Sipos, *J. Phys. Chem. B* 103 (1999) 11186–11190.
- [63] J. Patek, J. Hruba, J. Klomfar, M. Souckova, A.H. Harvey, *J. Phys. Chem. Ref. Data* 38 (2009) 21–29.
- [64] A.H. Narten, H.A. Levy, *J. Chem. Phys.* 55 (1971) 2263–2269.
- [65] A. Bard, L. Faulkner, *Electrochemical Methods: Fundamentals and Applications*, second ed., Wiley, 2000.
- [66] X. Wang, T.V. Nguyen, *J. Electrochim. Soc.* 155 (2008) B1085–B1092.
- [67] Q. Zhao, Y. Liu, C. Wang, *Appl. Surf. Sci.* 252 (2005) 1620–1627.
- [68] M.C. Kimble, *J. Electrochim. Soc.* 138 (1991) 3370–3382.
- [69] J.-H. Jo, S.-C. Yi, *J. Power Sources* 84 (1998) 87–106.
- [70] R. Faure, R. Durand, L. Genies, *Electrochim. Acta* 44 (1998) 1317–1327.
- [71] D. Sepa, M. Vojnovic, L. Vrancar, A. Damjanovic, *Electrochim. Acta* 31 (1986) 97–101.
- [72] D. Eberle, B. Horstmann, submitted for publication, 2014.
- [73] V. Yurkiv, A. Utz, A. Weber, E. Ivers-Tiffée, H.-R. Volpp, W.G. Bessler, *Electrochim. Acta* 59 (2012) 573–580.
- [74] T.A. Greszler, D. Caulk, P. Sinha, *J. Electrochim. Soc.* 159 (2012) F831–F840.
- [75] T. Suzuki, K. Kudo, Y. Morimoto, *J. Power Sources* 222 (2013) 379–389.
- [76] W. Lang, R. Zander, *Ind. Eng. Chem. Fundam.* 25 (1986) 775–782.
- [77] A.J. Elliot, M.P. Chenier, D.C. Ouellette, *Fusion Eng. Des.* 13 (1990) 29–31.
- [78] L. Jörissen, *J. Power Sources* 155 (2006) 23–32.
- [79] M.D. Koninck, B. Marsan, *Electrochim. Acta* 53 (2008) 7012–7021.
- [80] F. Cheng, J. Shen, B. Peng, Y. Pan, Z. Tao, J. Chen, *Nat. Chem.* 3 (2011) 79–84.
- [81] J. Park, X. Li, *J. Power Sources* 178 (2008) 248–257.
- [82] X. Niu, T. Munekata, S. Hyodo, K. Suga, *J. Power Sources* 172 (2007) 542–552.